In situ spectroscopic study of the plastic deformation of amorphous silicon under nonhydrostatic conditions induced by indentation

Y. B. Gerbig,[1,2,*] C. A. Michaels,[1] J. E. Bradby,[3] B. Haberl,[4] and R. F. Cook[1]

[1]*Material Measurement Laboratory, National Institute of Standards and Technology, 100 Bureau Drive, Gaithersburg, Maryland 20899, USA*

[2]*Mechanical Engineering Department, University of Maryland, College Park, Maryland 20742, USA*

[3]*Department of Electronic Materials Engineering, Research School of Physics and Engineering, Australian National University, Canberra 0200, Australia*

[4]*Chemical and Engineering Materials Division, Neutron Sciences Directorate, Oak Ridge National Laboratory (ORNL), 1 Bethel Valley Road, Oak Ridge, Tennessee 37831, USA*

(Received 26 August 2015; revised manuscript received 10 November 2015; published 17 December 2015)

Indentation-induced plastic deformation of amorphous silicon (a-Si) thin films was studied by *in situ* Raman imaging of the deformed contact region of an indented sample, employing a Raman spectroscopy-enhanced instrumented indentation technique. Quantitative analyses of the generated *in situ* Raman maps provide unique insight into the phase behavior of as-implanted a-Si. In particular, the occurrence and evolving spatial distribution of changes in the a-Si structure caused by processes, such as polyamorphization and crystallization, induced by indentation loading were measured. The experimental results are linked with previously published papers on the plastic deformation of a-Si under hydrostatic compression and shear deformation to establish a sequence for the development of deformation of a-Si under indentation loading. The sequence involves three distinct deformation mechanisms of a-Si: (1) reversible deformation, (2) increase in coordination defects (onset of plastic deformation), and (3) phase transformation. Estimated conditions for the occurrence of these mechanisms are given with respect to relevant intrinsic and extrinsic parameters, such as indentation stress, volumetric strain, and bond angle distribution (a measure for the structural order of the amorphous network). The induced volumetric strains are accommodated solely by reversible deformation of the tetrahedral network when exposed to small indentation stresses. At greater indentation stresses, the increased volumetric strains in the tetrahedral network lead to the formation of predominately fivefold coordination defects, which seems to mark the onset of irreversible or plastic deformation of the a-Si thin film. Further increase in the indentation stress appears to initiate the formation of sixfold coordinated atomic arrangements. These sixfold coordinated arrangements may maintain their amorphous tetrahedral structure with a high density of coordination defects or nucleate as a new crystalline β-tin phase within the a-Si network.

DOI: 10.1103/PhysRevB.92.214110 PACS number(s): 78.30.Am, 61.50.Ks, 78.30.Ly

I. INTRODUCTION

Fundamental differences in atomic bonding suggest that plastic deformation of amorphous covalent network materials should be treated separately from other groups of amorphous materials, such as metallic glasses and glassy polymers [1]. These latter materials have been the main focus of research on plastic deformation of amorphous materials in the last few decades. As a consequence, current knowledge of the mechanisms of plasticity in covalent materials is lacking [1,2]. In addition to wide use in electronic and semiconductor applications, amorphous silicon (a-Si) has become a model material for covalent amorphous network studies due to its simplicity [1–3]. Hence, a-Si has been intensively investigated with regard to dynamic and structural properties in theoretical and experimental studies [4–24]. However, the deformation behavior under external loads (e.g., hydrostatic pressure, shear stress, or a combination thereof) is only partially understood [2].

An early study on evaporated a-Si (in a supported taper apparatus) revealed a structural modification in the amorphous network with an increase in pressure [25]. The modification was inferred from *in situ* electrical measurements that detected a transition from semiconducting to metallic behavior [25]. Two possible mechanisms were proposed for the altered conductivity: (1) changes from tetrahedral bonding to greater coordination number metallic structures or (2) destruction of electronic localization with the tetrahedral coordination remaining intact [25]. Later diamond anvil cell (DAC) studies using *in situ* Raman spectroscopy and synchrotron x-ray diffraction (XRD) supported the former assumption. These studies proposed that a-Si undergoes a polyamorphic transition from a so-called low density amorphous (LDA) to a high density amorphous (HDA) state [26,27]. In some further DAC studies using *in situ* XRD, crystallization events were observed with [28,29] or without [30] a preceding polyamorphic transition during the compression of a-Si. The seeming conflict in these experimental results appears to have been resolved in a recently published paper by coauthors of the present paper [30]. In this paper, it was suggested that the extent of crystallization observed for a-Si under compression depends on the concentration of impurities: Crystallization is retarded or inhibited for a-Si samples with greater impurity content. However, in none of these experimental studies was the influence of hydrostatic versus deviatoric stresses on any

*Corresponding author: yvonne.gerbig@nist.gov

possible crystallization or amorphous-amorphous transition considered. Indeed, some DAC studies [26,27] did not use any pressure medium resulting in large pressure gradients and shear stresses [31]. Others [28,30] used methanol:ethanol, which is only hydrostatic for pressures less than ∼11 GPa [32], i.e., less than those for the onset of crystallization. No truly quasihydrostatic measurements using gases as pressure media have been performed on any form of a-Si, and the "true" hydrostatic phase behavior of a-Si thus remains unknown.

Deconvolution of hydrostatic and shear effects under pressure can be more readily achieved using modelling. For example, plastic deformation of a-Si has been investigated under pure shear stress conditions (volume-conserving plane strain) in molecular dynamics (MD) simulations [1,2,33–35]. Demkowicz and Argon proposed a model that included the existence of two distinct atomic environments, solidlike and liquidlike, in any given a-Si network [1,33,36]. The solidlike environment resembles the fourfold coordinated, diamond cubic (dc) Si structure. The liquidlike environment resembles a denser and fivefold coordinated liquid Si phase. In this model, solidlike atomic environments are transformed into liquidlike environments by spatially localized structural changes during shear deformation. The liquidlike environments decrease the resistance to plastic flow and act as a plasticity carrier in the amorphous network. Other studies confirmed a link between the systematic increase in the fraction of (fivefold) coordination defects and the occurrence of elementary plastic events in a-Si networks under shear deformation [2,34]. Shear stress creates liquidlike fivefold coordinated atoms that facilitate the constant reorganization of the amorphous network and thus increase structural disorder. Indeed, only thermal effects can establish a long range order (crystallization) in shear deformed a-Si according to some simulations [35]. In these simulations, only a combination of shearing and high temperatures (1000 K) initiates crystallization processes that follow closely the nucleation from the liquid phase and lead to the local formation of crystalline structures.

For hydrostatic compression, however, some simulations reported the onset of crystallization already at ambient temperatures [37]. In these simulations, hydrostatic pressure was found to reduce the differences in molar volume and coordination number between amorphous and crystalline Si phases. This, in turn, decreases the energy barrier to crystallization via solid state epitaxy [37]. As a consequence, the crystallization temperatures of metallic high pressure Si phases (β-tin, primitive hexagonal) decreased to room temperature with applied pressure [37]. This finding may offer an explanation for the occurrence of pressure-induced crystallization of a-Si at ambient temperatures under hydrostatic compression but not under pure shear deformation. In contrast, MD simulations under hydrostatic conditions have also observed the formation of higher density amorphous phases. In these studies, the transition from the LDA to the HDA state was described as driven by the creation of five- and sixfold coordinated defects [26,27,38,39]. In some cases, the formation of a very high density amorphous structure was observed, which was described as eight- and ninefold coordinated atomic arrangements within the tetrahedrally bonded network [38,39].

Investigations of plastic deformation of materials under stress conditions more complex than those found in pure hydrostatic compression or pure shearing are often conducted by indentation testing. In this technique, hydrostatic pressures and shear stresses are applied simultaneously to the sample. Indentation studies conducted on ion-implanted (as-prepared and annealed) a-Si revealed two competing mechanisms in the plastic deformation of a-Si: plastic flow and phase transformation [40]. The mode of deformation observed in an indentation experiment depends critically on the scale of the mechanical deformation [40] and structural order of the a-Si sample (determined by the preparation method and thermal history) [40–42]. A high degree of structural order and purity is usually required to initiate a phase transformation of a-Si to crystalline Si phases during indentation [43]. Highly disordered a-Si networks mostly deform via plastic flow [40]. Nonetheless, pure but defective as-implanted a-Si can transform into crystalline Si polymorphs under favorable "high load" conditions. This observation was confirmed on relaxed and as-implanted a-Si by indentation experiments coupled with *in situ* electrical contact resistance measurements. The experiments revealed a pressure-induced semiconductor-to-metal transition in a-Si during indentation loading [40,44,45], similar to the observations in DAC studies [25,27]. However, unlike the cited DAC studies, the contact region between the indenter probe and sample was not readily accessible to analyze *in situ* the structural transitions causing the observed alterations in conductivity. Nonetheless, two possible scenarios were suggested regarding the underlying phase transitions during indentation loading [40,45,46]: (1) densification to the HDA phase (in analogy to DAC compression studies of a-Si) or (2) crystallization to the β-tin phase (in analogy to DAC compression studies of dc Si). Indeed, a MD simulation of a-Si under indentation pressure suggested the formation of sixfold coordinated atoms as the cause for the change in conductivity [47] and, thus, seems to confirm the former assumption. However, prior to the paper here, experimental evidence relevant to this question was not available.

In order to directly analyze indentation-induced structural and phase changes in materials, Raman spectroscopy has been combined with instrumented indentation testing (IIT) in a method called Raman spectroscopy-enhanced IIT. This innovative method enables the *in situ* spectroscopic analyses of mechanically deformed regions under contact loading. In this paper, Raman spectroscopy-enhanced IIT in an *in situ* Raman mapping configuration is employed to study the evolution of the plastic deformation of a pure, voidless a-Si thin film during indentation loading. Raman spectroscopy is an extremely powerful tool for the structural characterization of a-Si, as this technique is very sensitive to changes in the amorphous network, e.g., Refs. [4,13,14,27,43]. DAC experiments using *in situ* XRD or Raman spectroscopy are not easily conducted on pure, voidless a-Si and have so far not been reported. This lack is mainly due to the fact that relatively large quantities of test material are required in such experiments. The *in situ* Raman mapping capability in this paper enables assessment of the localized nature of deformation and transformation of a-Si under load across the deformation zone that is not easily possible with bulk XRD measurements in DACs.

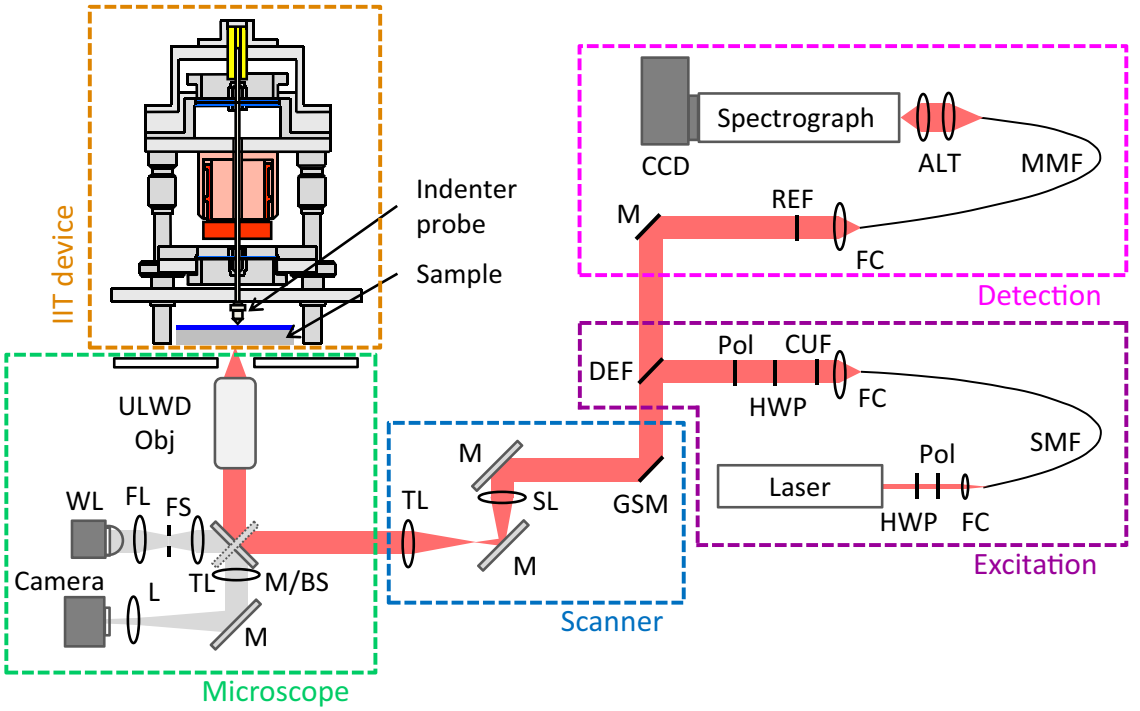

FIG. 1. (Color online) Schematic diagram of the optical layout for the laser scanning Raman microscope component of the Raman spectroscopy-enhanced IIT device: ALT = achromatic lens telescope, BS = beamsplitter, CCD = charge-coupled device, CUF = clean-up filter, DEF = dichroic edge filter, FC = fiber coupler, FL = field lens, FS = field stop, GSM = galvanometer scan mirrors (two axis), HWP = half-wave plate, L = lens, M = mirror, MMF = multimode fiber, Pol = polarizer, REF = Raman edge filter, SL = scan lens, SMF = single mode fiber, TL = tube lens, ULWD Obj = ultralong working distance objective, and WL = white light.

II. EXPERIMENTAL DETAILS

A. Experimental setup

Indentation experiments coupled with *in situ* Raman imaging were conducted on as-implanted a-Si thin films using Raman spectroscopy-enhanced IIT. This technique was developed at the National Institute of Standards and Technology (NIST) and has been described in detail in previous publications [48,49]. A schematic diagram of the experimental setup is shown in Fig. 1 and is described briefly in the following section.

Raman spectroscopy-enhanced IIT employs an in-house built IIT device that is coupled with a custom laser scanning Raman microscope. The purpose of this experimental setup is to conduct *in situ* spectroscopic analyses of mechanically deformed regions of optically transparent materials under contact loading. The force transducer of the IIT device allows adjustment of experimental parameters, such as indentation loads and (un)loading rates. An incorporated displacement sensor allows for collection of force-displacement data comparable to conventional IIT instruments. The IIT device, along with a specimen holder featuring an aperture in the center, is mounted on the XY translation stage of an inverted optical microscope. That microscope is configured for Raman microscopy, allowing optical access to the mechanically deformed regions of transparent samples.

An early version of the Raman microscope, in which only the acquisition of point spectra (*in situ* Raman microprobing) was possible, has been described in some detail in an earlier publication [48]. The current configuration of the microscope includes the capability to perform *in situ* Raman mapping of the sample-probe contact region while under load. The additions to the microscope associated with the introduction of this new capability were reported in a subsequent publication [49].

B. Test specimen

The *in situ* tests were performed on a-Si thin films on sapphire substrates (a-SoS). Silicon on sapphire specimens, 20 mm × 20 mm, were cut from a sapphire r-plane wafer (wafer thickness: 530 μm ± 50 μm, polished on both sides), which was deposited with an epitaxially grown Si(100) film (film thickness: 600 nm ± 60 nm). The surface normal of the sample was misaligned by 5° ± 1° with respect to the ⟨001⟩ direction of the Si film. The cut edges of the sample were misaligned by 3.5° ± 1° with respect to the directions ⟨110⟩ and $\langle 1\bar{1}0\rangle$ of the film, as shown by electron backscattered diffraction measurements. Uncertainties represent intrinsic measurement errors and mounting errors.

The a-SoS specimens were obtained by Si ion implantation-induced amorphization of SoS specimens. The Si self-ion implantation was carried out using the Australian National University 1.7 MeV tandem high-energy ion implanter (NEC, Middleton, Wisconsin) [50] at liquid nitrogen temperature. The following fluences and energies were utilized at a tilt of 7° to the sample surface normal:

(1) 1×10^{15} ions/cm^2 with 80 keV;
(2) 3×10^{15} ions/cm^2 with 250 keV.

These implantation conditions are well known to result in a fully amorphized surface layer. The ion-implanted samples were not annealed and were tested in their unrelaxed state. Raman spectroscopy revealed no peak related to the initial dc structure of Si after the ion implantation process, consistent with a fully amorphized Si film. (Sputtered a-Si films contain impurities and nanostructure that cannot be eradicated by thermal annealing and change the high pressure and mechanical behavior [51,30]. The purity and absence of voids in implanted films as used here has been well documented, e.g., Ref. [52].)

C. Indentation experiment

A series of Raman images from the contact region between the indenter probe and sample was collected at increasing contact loads in stepped indentation experiments. In these experiments, the indenter probe was brought into contact with the sample. A load was applied (L1 = 38 mN) and held constant for the time required to collect the Raman image of the region of interest (ROI). The applied indentation force was then increased (loading rate 5 mN/s) to a load L2 = 78 mN, and a second Raman image of the same ROI was acquired. The indentation loads were increased three more times (to L3 = 118 mN, L4 = 239 mN, and L5 = 440 mN, at a loading rate 5 mN/s). The indentation displacements measured at the applied loads were 86 nm (L1), 147 nm (L2), 194 nm (L3), 302 nm (L4), and 458 nm (L5). The indentation stress, p_i, at the various loads was calculated from the load and displacement data [49]. It was determined as approximately 3.5 GPa (L1), 5.4 GPa (L2), 6.2 GPa (L3), 8.1 GPa (L4), and 9.8 GPa (L5). A Raman image was recorded at each of the loading steps. The indenter probe used in the experiments was a conospherical diamond with a nominal tip radius of 45 μm.

A limited number of indentation experiments were conducted in which the contact region between the indenter probe and sample was imaged while a load was applied and then after completely unloading from that load. This set of Raman data (loaded and unloaded) was collected for indentation forces L1 and L3.

D. *In situ* mapping

To collect an *in situ* Raman image, a 20 μm × 20 μm ROI was scanned. Twenty individual spectra were collected at evenly spaced locations along the 20 μm scan range in each direction, generating a 20 × 20 hyperspectral dataset. A custom LabVIEW (Austin, Texas) [50] code was used to synchronize the laser scanner positions with the spectral acquisition. The collection time for an individual Raman spectrum was set to 15 s. (Although these images took several hours to acquire, tests of displacement and force stability indicated that the system is sufficiently robust to perform such measurements.) The Raman measurements were all recorded with an 80× ultralong working distance metallurgical objective (Olympus, Waltham, Massachusetts) [50] with a numerical aperture of 0.75. Focusing through the sapphire substrate is clearly not the ideal use of a metallurgical objective. Thus, the lateral resolution was undoubtedly degraded below the diffraction limited value (≈520 nm) that might be achieved with this objective. A qualitative assessment of the recorded Raman images suggested lateral resolution of approximately 1 μm. The degraded depth resolution is of little consequence as the Si layer thickness is significantly smaller than the depth of field of this objective even in the absence of the sapphire. The nominal illumination power of the 785 nm light source was set to 5 mW at the sample surface.

III. ANALYSIS OF RAMAN SPECTRA

A. Fitting

A custom spectroscopic image analysis program written in IDL (Exelis, McLean, Virginia) [50] was employed for fitting the individual Raman spectra. The Raman spectra from each pixel were fit to a model spectrum consisting of a series of bands of Gaussian lineshape using a conventional nonlinear least squares algorithm. The analysis resulted in maps of the amplitude, center wavenumber, and full width, half maximum (FWHM) for each band. The spectral range less than 200 cm^{-1} was affected by the performance characteristics of the long pass Raman edge filter. Consequently, the transverse acoustic (TA) peak of a-Si (located at around 180 cm^{-1}) could not be reliably fit and no spectral data are given for this peak in the paper. For the other relevant Si modes, the Raman spectra fit over the range 200 cm^{-1} to 700 cm^{-1} were used for a detailed quantitative analysis. From the resulting hyperspectral data cube, two-dimensional color fill contour images (Raman maps) were formed, which showed the spatial variation of specific features of individual Raman peaks (see Sec. III B).

B. Relative Raman shift, relative peak width, intensity ratio

For easier comparison of data recorded at different stages during the experiment, the following relative values rather than absolute spectral parameters were evaluated.

The relative Raman shift $\Delta\omega_x$ of a fitted Raman band x at an individual collection point i of the Raman map (i = 1 to 400) is

$$\Delta\omega_x = \omega_{i,x} - \overline{\omega_x}, \tag{1}$$

where $\omega_{i,x}$ is the center wavenumber for that band and $\overline{\omega_x}$ is the average center wavenumber for the mode in the remote pristine state.

The relative FWHM $\Delta\Gamma_x = \Delta\mathrm{FWHM}_x$ of the fitted Raman band x at an individual collection point i of the Raman map is

$$\Delta\Gamma_x = \Delta\mathrm{FWHM}_x = \mathrm{FWHM}_{i,x} - \overline{\mathrm{FWHM}_x}, \tag{2}$$

where $\mathrm{FWHM}_{i,x}$ is the peak width for that band and $\overline{\mathrm{FWHM}_x}$ is the average peak width for the mode in the remote pristine state.

To obtain reference data for the remote pristine (unindented) amorphous sample, the average values for wavenumber and peak width ($\overline{\omega_x}$, $\overline{\mathrm{FWHM}_x}$) were determined by averaging the appropriate data from the first and last rows as well as the first and last columns of the 20 × 20 hyperspectral dataset, i.e., sample regions that lie well outside the deformation zone of the tip-sample contact.

The intensity ratio of the transverse optical (TO) band, $I_{i,y/\mathrm{TO}}$ [y = longitudinal optical (LO) or longitudinal acoustic (LA)] at an individual collection point was determined as the ratio between the absolute intensity of the TO band, $I_{i,\mathrm{TO}}$,

band and the absolute intensity of the LO or LA band, $I_{i,y}$ (y = LO, LA), for that point, respectively.

C. Bond angle distribution

The degree of local order in fully amorphous, pure Si is related to the distribution of the distorted bond angles compared to perfect tetrahedrally bonded crystalline Si [18].The bond angle distribution $\Delta\theta$ is the standard deviation of the bond angles in a given sample volume [17]. Several theoretical relationships between the bond angle distribution $\Delta\theta$ and the half-width $\Gamma/2$ of the TO peak (a-Si) have been proposed in previous papers [4,13,18,20,22,24]. A critical review by Roura *et al.* showed that these relationships can be basically grouped [53], either around the correlation suggested by Vink *et al.* [20] or the Beeman-Tsu formula [4]. However, a slightly better agreement was found between the theoretical results obtained with the Beeman-Tsu relationship and direct measurements of $\Delta\theta$ [53].The current authors are aware that the use of any of the proposed correlations for calculating the absolute value of $\Delta\theta$ should be performed with caution [53]. Nonetheless, for the purpose of comparison with other papers, calculations of the bond angle distribution $\Delta\theta_i$ for an individual point i in the Raman map were included in this paper based on the Beeman-Tsu formula [53]:

$$\Delta\theta_i = [(\Gamma_i/2) - 7.5]/3. \tag{3}$$

To replicate the spectral analysis in the original paper by Beeman *et al.* [4], $\Gamma_i/2$ was taken as the half-width of the spectral feature related to the TO peak in the cumulative fitted Raman spectrum. The half-width was taken on the high wavenumber side at half the maximum height of spectral feature. This was done to minimize the influence of a-Si Raman peaks overlapping the low wavenumber side on the width calculation, as indicated in Fig. 2.

D. Volumetric strain

The wavenumber of an individual vibrational mode depends on the density or molar volume of the material. The mode Grüneisen parameter γ_x for mode x measures how sensitive the wavenumber ω is to changes in molar volume V and is defined as

$$\gamma_x = -\partial ln\omega/\partial lnV = -(V_i/\omega)\cdot(\delta\omega/\delta V_i), \tag{4a}$$

where $\delta\omega$ and δV_i are the changes in the wavenumber and molar volume, respectively, at location i relative to a reference location. Rearranging Eq. (4a) to expression (4b), enables variations in the wavenumber of the TO mode for an individual point i of the Raman map to be associated with the volumetric strain $\varepsilon_{V,i}$ at that that point:

$$\delta V/V = -1/\gamma_{\mathrm{TO}}\cdot(\delta\omega_{\mathrm{TO},i}{}^*/\overline{\omega_{\mathrm{TO}}}) = \varepsilon_{V,i}. \tag{4b}$$

In the rearrangement of the mathematical expressions, γ_x in Eq. (4a) was substituted by the mode Grüneisen parameter for the TO mode, γ_{TO}, in Eq. (4b), ω was substituted by the average wavenumber of the TO mode, $\overline{\omega_{\mathrm{TO}}}$, and $\delta\omega$ was substituted by the change in the wavenumber of that mode, $\delta\omega_{\mathrm{TO},i}{}^*$, for point i.

For this paper, the value of γ_{TO} was taken as 0.8, based on the paper by Fabian and Allen [5]. The parameter $\overline{\omega_{\mathrm{TO}}}$ was calculated, as explained in Sec. III B. The wavenumber change $\delta\omega_{\mathrm{TO},i}{}^*$ considered in Eq. (4b) is the shift of the TO band due to volume changes of the a-Si. In the case of indentation, volume reduction (densification) of the a-Si is expected due to compression beneath the contact between the indenter probe and sample. Densification of the a-Si causes shifts of the TO band to higher wavenumbers (positive shift) [5,6]. In addition to densification, an increase of structural disorder can also be anticipated during the exposure of a-Si to mechanical stress [26,38]. An increase in the structural disorder of a-Si reportedly leads to shifts towards lower wavenumbers (negative shift) [6,9,12,13,23,54]. Evidence for the occurrence of both of these counteracting mechanisms was found in this paper. Therefore, the observed relative Raman shift of the TO band ($\Delta\omega_{\mathrm{TO},i}$) at an individual point i in the Raman map is the sum of the Raman shift of the TO band due to volume densification (magnitude $\Delta\omega_{\mathrm{TO,vol},i}$) and the opposing shift due to increase in the structural disorder (magnitude $\Delta\omega_{\mathrm{TO,dis},i}$)

$$\Delta\omega_{\mathrm{TO},i} = \Delta\omega_{\mathrm{TO,vol},i} - \Delta\omega_{\mathrm{TO,dis},i}. \tag{5a}$$

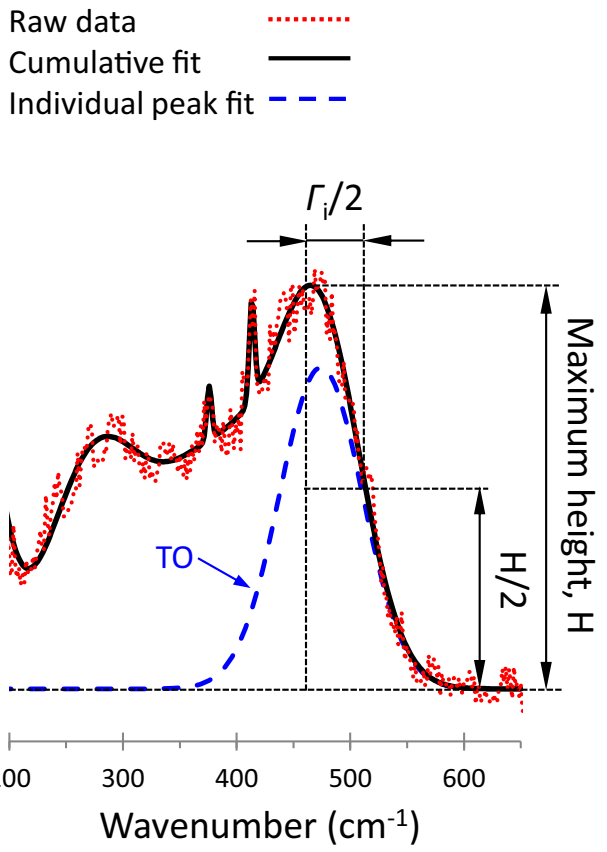

FIG. 2. (Color online) Determination of the parameter $\Gamma_i/2$ from a fitted cumulative Raman spectrum. The parameter $\Gamma_i/2$ represents the half-width at the higher wavenumber side at half the maximum height ($H/2$) of the spectral feature related to the TO peak in the cumulative fit (solid line) of the collected Raman spectra (raw data, dotted line). The cumulative fit was obtained by superposition of the fits for the individual a-Si peaks. For example, the individual fit for TO peak is shown as a dashed line.

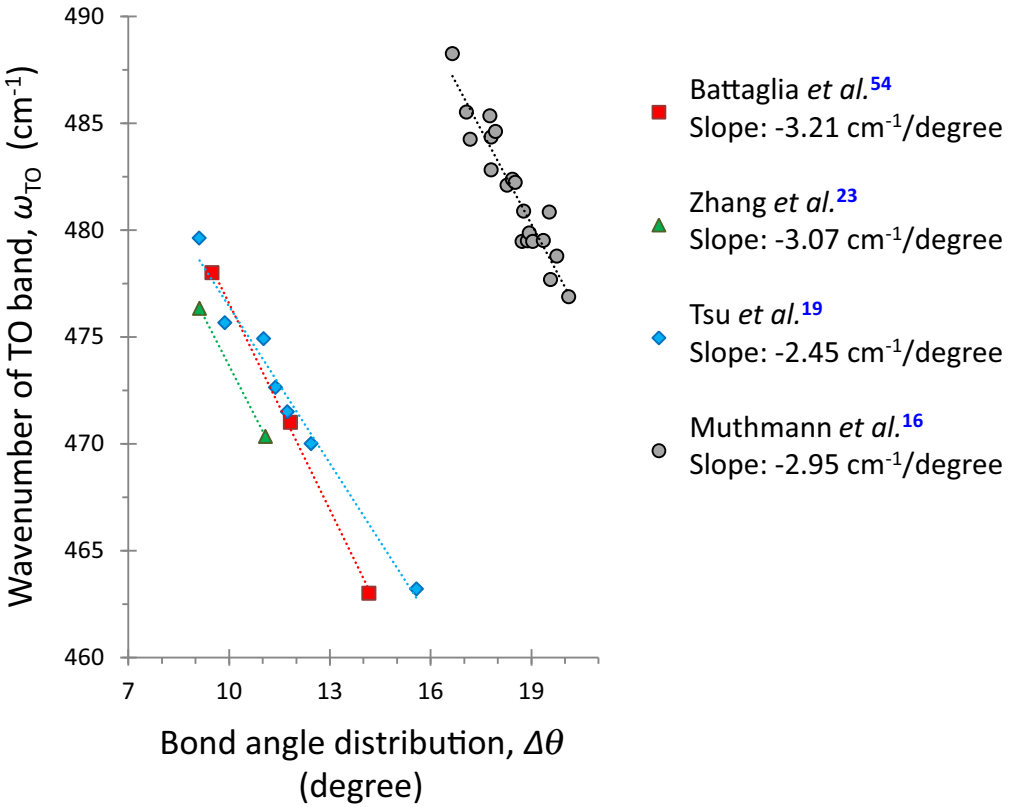

FIG. 3. (Color online) Raman shift of the TO band as a function of the bond angle distribution as reported by various groups.

Hence, the wavenumber change of the TO band for point i can be calculated as

$$\delta\omega_{\mathrm{TO},i}{}^{*} = \Delta\omega_{\mathrm{TO,vol},i} = \Delta\omega_{\mathrm{TO},i} + \Delta\omega_{\mathrm{TO,dis},i}\,. \tag{5b}$$

The shift due to structural disorder was estimated in the following way. Based on various datasets published in previous studies [16,19,23,54], the wavenumbers of the TO band were plotted as a function of the bond angle distribution (a measure of the structural disorder) for samples exhibiting different degrees of disorder (Fig. 3). The data sets were then fit with linear equations. The slopes of the linear fits correlated the relative Raman shifts to the relative bond angle distribution. The values for the slope obtained for the different data sets were averaged. The averaged slope value $(-2.9 \pm 0.3)\,\mathrm{cm}^{-1}$/ degree was then used to determine $\Delta\omega_{\mathrm{TO,dis},i}$ for an individual point i of the Raman map:

$$\Delta\omega_{\mathrm{TO,dis},i} = -2.9 \cdot \Delta\theta_i{}^{*}, \tag{6}$$

where $\Delta\theta_i{}^{*}$ is the relative bond angle distribution (in degrees) at an individual collection point i of the Raman map,

$$\Delta\theta_i{}^{*} = \Delta\theta_i - \overline{\Delta\theta_i}, \tag{7}$$

where $\overline{\Delta\theta_i}$ is the average bond angle distribution for the mode (pristine state). The average value was determined by averaging the appropriate data from the first and last rows as well as first and last columns of 20×20 hyperspectral dataset. $\Delta\theta_i$ was calculated with Eq. (3).

IV. RESULTS

Figure 4(a) shows a fitted Raman spectrum taken from the pristine a-SoS sample before testing. The individual peaks and bands are indicated as dotted lines. All of the main bands of the a-Si sample Raman spectra from 100 cm^{-1} to 600 cm^{-1} are shown in Fig. 4(a), including the TA mode. The fitted spectra are displayed for purposes of clarity. The raw spectra contain high frequency noise due to spectroscopic etaloning that impedes visual examination of the changes in the broad a-Si bands. While the spectroscopic etalon noise is independent of the data acquisition time, shot noise is a significant component of the overall spectral noise. Increasing spectral acquisition times would lead to less shot noise, but this has to be balanced against the time required to record the entire load-unload mapping sequence. The acquisition time (15 s per pixel) utilized here was chosen to yield reasonable quality spectra in an overall measurement scheme of practical duration. Figure 4(b) displays a Raman spectrum taken inside the contact zone between the indenter probe and a-SoS sample at load L1 (left), an image of spatial variations in the relative Raman shift of the TO band (middle) and an image of the spatial variation of the relative width of the TO band (right). The square added to the Raman map indicates the spatial location of the pixel from which the spectrum originates.

Figures 4(c)–4(f) are organized in the same fashion as Fig. 4(b). The Raman spectra in these figures were taken consecutively at the same location as Fig. 4(b) and show the progression of the changes in the spectrum of the a-Si thin film in this particular location during further loading (L2 to L5). The images are plotted with color scales that facilitate observation

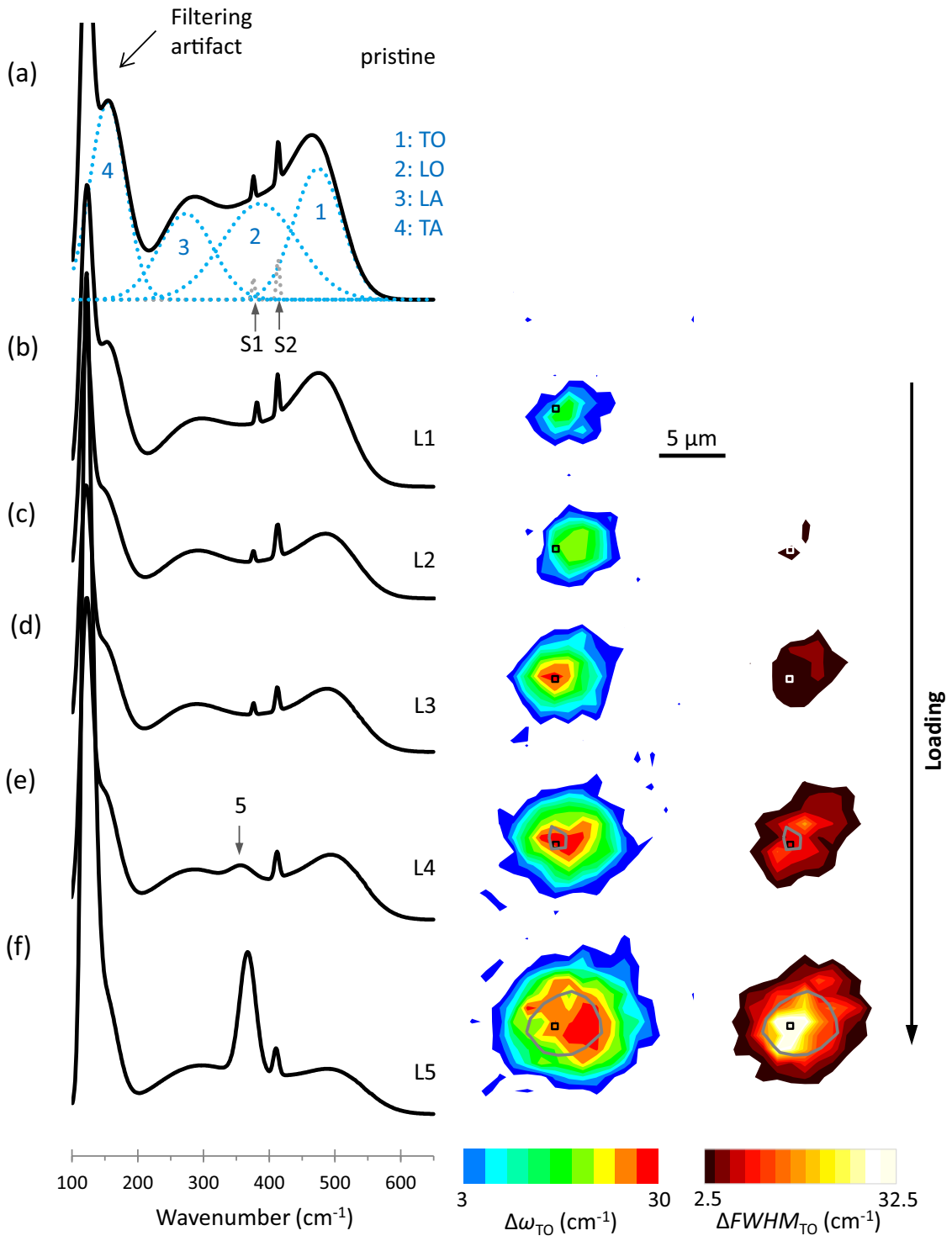

FIG. 4. (Color online) (a) Fitted Raman spectrum of the pristine a-SoS sample before testing showing the individual Raman bands of a-Si (1 to 4) and Raman peaks originating from the sapphire substrate (S1 and S2). (b)–(f) Raman spectra taken inside the contact zone between the indenter probe and a-SoS sample at various loads (left), images of spatial variations in the relative Raman shift of TO band (middle), and images of the spatial variation of the relative width of TO band (right) in the contact zone. The squares added to the Raman maps indicate the location of the data point resulting in the spectrum shown. (e) and (f) An additional peak (5) was detected in the Raman spectra. The outline of the region, where peak 5 was detected, is indicated as dark gray contour plots in the corresponding Raman images.

of the changes in the spectral parameters in the contact area: Standard deviations of the reference values, $\overline{\omega_{\mathrm{TO}}}$ and $\overline{\Gamma_{\mathrm{TO}}}$ [Eqs. (1) and (2)], were first determined from a data subset consisting of the first and last rows as well as the first and last columns of the 20 × 20 hyperspectral dataset. The color maps of the relative Raman shift, $\Delta\omega_{\mathrm{TO}}$, and the relative peak width, $\Delta\Gamma_{\mathrm{TO}}$, of the TO band in Fig. 4 were then generated as follows. The lower levels were set by (a reference value − twice

the standard deviation of a reference value). The step sizes were set by (twice the standard deviation of a reference value). The upper level of the image scales was dependent on the greatest value determined for $\Delta\omega_{TO}$ or $\Delta\Gamma_{TO}$, respectively. In this way, white areas in the maps indicate no significant change in a spectral quantity from the pristine state. In the Raman images taken at L4 and L5, the dark gray contours indicate the region where peak 5 was detected. The boundary of the contour for peak 5 represents the minimum intensity of this peak that is required for reliable detection under the experimental conditions used.

The Raman spectrum of a-Si is characterized by four broad bands with center wavenumbers as indicated: TO (480 cm^{-1}), LO (380 cm^{-1}), LA (near 300 cm^{-1}), and TA (between 80 cm^{-1} and 200 cm^{-1}) [21]. The TO band is caused by TO phonons associated with Si-Si stretching vibrations within a tetrahedrally bonded network [14,39]. Contributions by longitudinal phonons cause the formation of the LO band, which is usually observed as a low frequency shoulder on the TO band [55]. The LA band is associated with tetrahedral bending modes but also contains contributions from acoustic overtones and combination (TO + TA) modes [55]. The TA band is mainly assigned to TA vibrations [55] and is bond bending in nature [14,39]. As indicated in the Raman spectrum of the pristine sample [Fig. 4(a)], band 1 in the spectrum was identified as TO mode, band 2 as LO mode, band 3 as LA mode, and band 4 as TA mode. As mentioned earlier, the detection of the TA mode is affected by a measurement artifact induced by the long pass Raman edge filter. Additionally, two narrow peaks S1 and S2 (labeled S for substrate) detected at 418 cm^{-1} and 378 cm^{-1} are related to the A_{1g} or E_g modes of the sapphire substrate, respectively [56].

As the most distinct band of the spectrum and highly sensitive to local tetrahedral symmetry of a-Si [12,14,15], the correlation between spectral parameters of the TO band and the structure of the a-Si has been widely studied, e.g., Refs. [4,6,13,18,20]. Hence, the analysis of the Raman spectra collected in this paper will primarily focus on the TO band of a-Si.

On application of the first indentation load L1 [Fig. 4(b)], the intensity of the overall Raman signal was reduced compared to the Raman spectrum of the pristine sample [Fig. 4(a)]. More importantly, the mechanical stress induced by the indentation caused a shifting of the TO band from an initial averaged value of 470.1 cm^{-1} towards higher wavenumbers. In the Raman map, shifts are observed in a circular pattern, indicating the contact area between indenter probe and sample. A circular contact area was expected due to the nature of the contact geometry (conosphere on flat). Consequently, the largest wavenumber shifts are located in the center of the contact area, where the predicted hydrostatic pressure is the greatest. The width of the TO band was not significantly altered from an initial averaged value of 88.3 cm^{-1} under the applied load. The width of the TO band is comparable to other a-Si samples prepared by ion implantation [57]. As the variations in the relative width do not exceed the lower threshold of the image scale, no data points are shown in the corresponding map.

On loading to L2 and greater loads, the TO band broadened considerably, as seen in the Raman spectra shown in Figs. 4(c)–4(f). The broadening of the TO band was previously linked to an increase of local strain [4,13,18] due to increasing intrinsic changes in the short-range order [8,11,19]. Also, the relative Raman shift of the TO band became more pronounced as the band shifts continuously towards higher wavenumbers with further loading. As previously mentioned (see Sec. III D), the center peak position of the TO band may be influenced by densification processes (shifting towards higher wavenumbers) in addition to disorder effects (shifting towards lower wavenumbers) imposed in the a-Si. However, the densification process appear to be more dominant than the disorder effect, as positive Raman shifts of the TO band were continuously recorded. The broadening and hardening of the TO band observed in this paper are similar to observations reported for DAC experiments [8,27,28,55] and related simulation studies [39,55]. The Raman images in Figs. 4(c)–4(f) show that the circular contact area between probe and sample increased steadily with greater loads. The largest Raman shifts of the TO band were observed in the center of the contact area. Furthermore, the width of the TO bands was significantly altered starting from L2. Initially, broadening of the TO band was observed only in two small separate regions but then extended over a continuous zone growing with greater loads.

In addition to these changes observed in the amorphous structure, at loads L4 and L5, a new peak (5) located at around 360 cm^{-1} appeared in the Raman spectra of Figs. 4(e) and 4(f). With increasing load, the intensity of peak 5 increased, and the region where peak 5 was detected expanded.

Comparing the Raman spectra taken at different loads (Fig. 4) reveals changes in the intensity of the TO band, especially in relation to the LA longitudinal bands. Examples for the quantitative alteration of the relative intensity ratio of the two longitudinal bands LA ($I_{LA/TO}$) and LO ($I_{LO/TO}$) to the TO band are shown in Fig. 5. Figure 5(a) shows a gray scale image of the intensity distribution of the TO band under the first contact load L1. The dark colored circular area marks the contact zone between the indenter probe and the amorphous film. The row colored in yellow indicates the position of the line of data included in the charts of Figs. 5(b) and 5(c). For reference, the red square marks the location of the Raman spectrum shown for load L1 in Fig. 4(b). Figure 5(b) shows the relative intensity ratios along the line indicated in Fig. 5(a) for loads L1 to L5. As can be seen, the amplitude (intensity) of the TO band diminishes significantly with increasing load relative to the other Raman bands, consistent with DAC experiments [27,28,55]. The loss in intensity of the TO band is another sign of the increasing disorder [6] on the nearest neighbor scale induced in the a-Si film during indentation.

Although this paper focuses mainly on the analysis of the TO band, a few observations about the other bands of a-Si are worth mentioning. Figure 5(c) shows the relative Raman shifts for LA and LO bands along the line indicated in Fig. 5(a) for the various loads. It was observed that the wavenumber of the LO bands shifted to higher values when exposed to increasing loads inside the contact region. Similar observations for this band have been reported in a DAC study [8] and related simulations [39]. In the case of the LO band, both effects and volume reduction (densification),

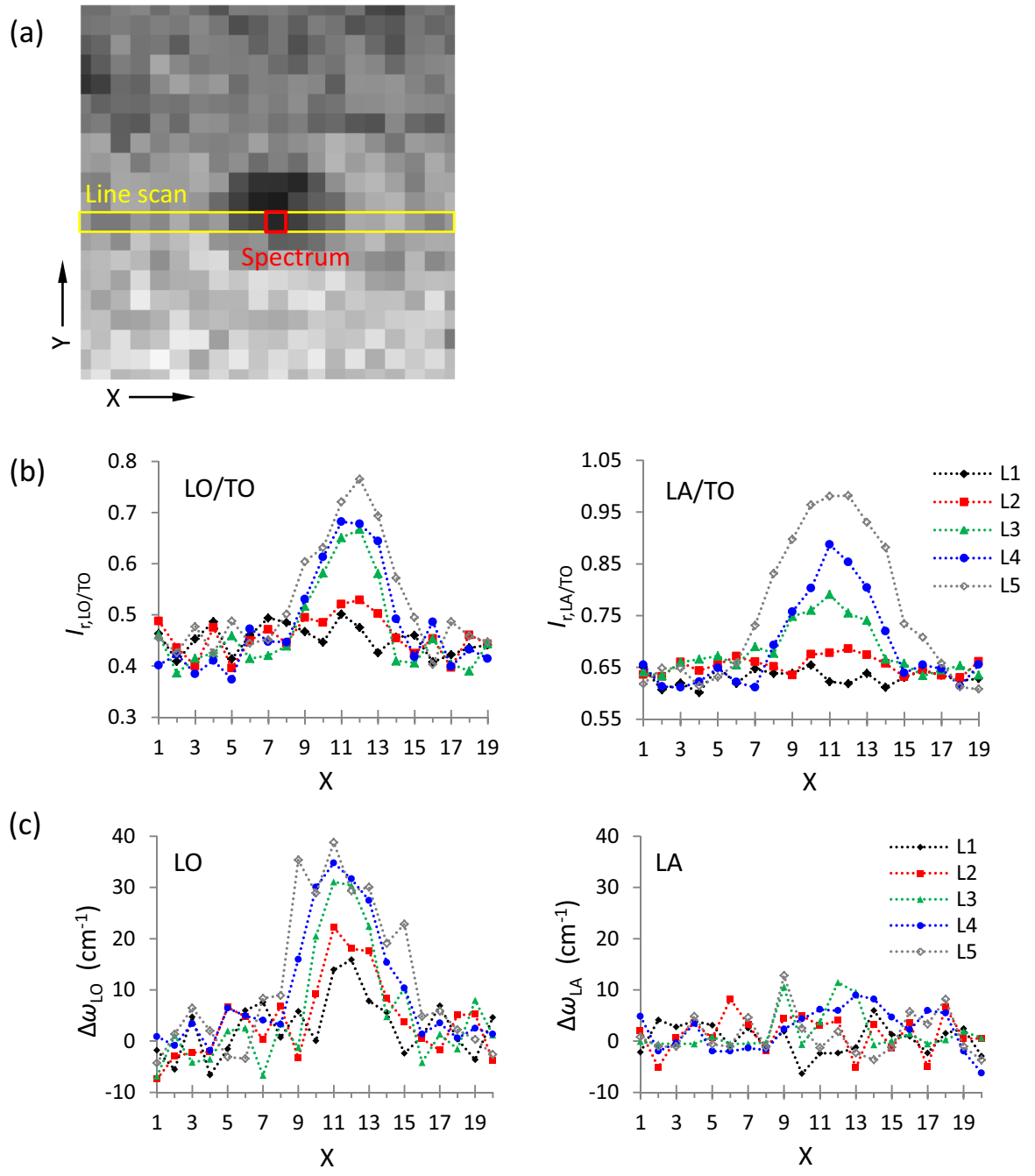

FIG. 5. (Color online) (a) Gray scale image of the intensity distribution of the TO band under the first contact load L1. The yellow row indicates the position of the line of data included in the charts in 5(b) and 5(c). For reference, the red square marks the location of the Raman spectrum shown for load L1 in Fig. 4(b). (b) Plot of the relative intensity ratios $I_{r,LO/TO}$ and $I_{r,LA/TO}$ along the line indicated in Fig. 5(a) for loads L1 to L5. (c) Plot of the relative Raman shifts for the LA and LO bands along the line indicated in Fig. 5(a) for the loads L1 to L5.

as well as an increase of the disorder, induce Raman shifts towards higher wavenumbers [6,39]. The position of the LA band remains mostly unchanged, as also observed in the DAC study conducted by Ishidate *et al.* [8]. As mentioned earlier, a quantitative analysis of the TA band was not possible due to experimental restrictions. However, a qualitative assessment can be made from the comparison of the Raman spectra in Figs. 4(a)–4(f). It revealed an apparent shift of the TA band towards lower wavenumber under increasing load. The softening of the TA mode under pressure [8,39] has been attributed to the negative mode Grüneisen parameter for that mode [5].

The observed changes in the TO band can be related to volumetric strains, $\varepsilon_{V,i}$ via the mode Grüneisen parameter, as detailed in Sec. III D. The induced strains (distortions) of the Si tetrahedra cause large deviations of the Si-Si-Si bond angles from the ideal value of approximately 109° [17,24], described by the bond angle distribution $\Delta\theta_i$ (Sec. III C). Color contour images (20 μm × 20 μm) of the spatial distribution of

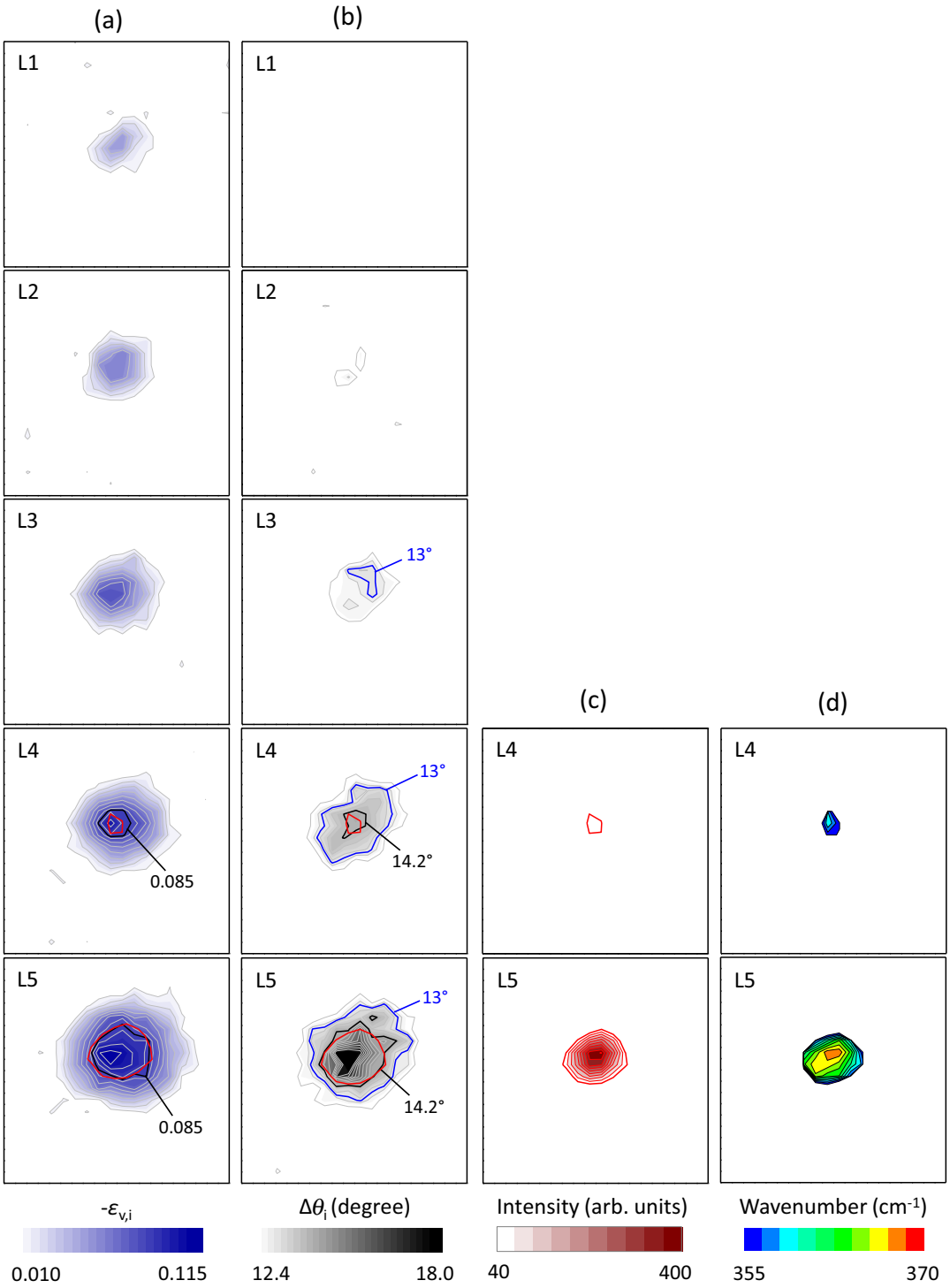

FIG. 6. (Color online) Raman maps imaging the spatial variation in (a) the negative (compressive) volumetric strain, $\varepsilon_{V,i}$ (left image), and (b) the bond angle distribution, $\Delta\theta_i$ (right image), for the various indentation loads L1 through L5. Additionally, red contour lines are plotted to indicate the regions, where peak 5 was detected. The lower boundary of the contour plot of peak 5 represents the intensity count of 40, which was the minimum intensity of this peak required for reliable detection under the experimental conditions in this paper. The intensity and wavenumber of peak 5 are shown in Figs. 6(c) and 6(d), respectively.

volumetric strain and the bond angle distribution in the contact area between the indenter probe and a-SoS sample are shown in Figs. 6(a) and 6(b) for all loading stages of L1 through L5. As above, the images are plotted with color scales that facilitate observation of changes in the structural parameters in the contact area. In this case, the color maps of Fig. 6 were generated as follows: The lower levels were set by (a reference value − one standard deviation of a reference value). The step sizes were set by (one standard deviation of a reference value). As before, the upper levels of the image scales were dependent

on the greatest value determined for $\varepsilon_{V,i}$ or $\Delta\theta_i$, respectively. The reference values and standard deviations were determined from a data subset well outside the contact area. Additionally, red lines are plotted to outline the regions where peak 5 was detected, i.e., at loads L4 and L5. The boundary of the contour for peak 5 represents the minimum intensity of this peak that is required for reliable detection under the experimental conditions used. More detailed information about intensity and wavenumber of peak 5 are shown in the contour plots of Figs. 6(c) and 6(d), respectively.

Indentation of the a-SoS film induced negative volumetric strains. With increasing indentation load, greater absolute values for strain were determined in the contact zone. For strain values less than 0.05 (at L1), no significant changes in the bond angle distribution (average $\pm$ standard deviation: $12.2^\circ \pm 0.2^\circ$) were detected. At strains around 0.055 (at L2), slight, localized changes ($\approx 0.5^\circ$) in the bond angle distribution were found in the contact area. This indicates an increase in the structural disorder within the amorphous network. Together with further increase in strain, the degree of the disorder and the area affected thereby also grew (L3 through L5). At load L4, a new mode, peak 5, was observed in the Raman spectrum [see Fig. 4(e)]. The new peak 5 (observed at L4 and L5 in the Raman spectra [Figs. 4(e) and 4(f)]) cannot be associated with any known Raman modes of the amorphous Si phase, which suggests the formation of a new Si phase and the onset of a phase transition. The relatively narrow peak width [see Fig. 4(f)] indicates that this phase is probably of crystalline rather than amorphous nature. It might be argued that impurities or segregation from the sapphire substrate caused this newly observed spectral feature. However, no impurity (especially oxygen) movement is expected in the current a-Si system, sapphire does not easily decompose under pressure, and the system was not heated significantly. Furthermore, even if a reaction with Si had taken place, an increase in overall luminescence rather than a narrow peak would have been expected [58]. Peak 5 is thus attributed to a new structure of Si evolving under indentation loading.

A superposition of the intensity plots of peak 5 and the maps for volumetric strain and bond angle distribution suggests that the new phase was detected only in regions of strains of at least 0.085 and bond angle distributions of at least 14.2°. As those regions expanded with increasing indentation load (from L4 to L5) so did the detected areas of the new phase. This observation indicated the crystallization of a growing portion of the strained amorphous material in the contact zone. Furthermore, it can be observed that the intensity of peak 5 significantly increased together with a shift to larger values at L5 [Fig. 6(d)] compared to L4 [FIG. 6(c)].

In situ Raman imaging experiments were conducted in which the contact region between indenter probe and sample was imaged under load and after completely unloading from loads L1 and L3 (see Sec. II C). From the fitted spectral data, maps of the relative Raman shift of the TO band and the bond angle distribution were plotted and compared for the loaded and unloaded state for each load. The comparison showed that permanent changes in the spectral features of a-Si, defined, here as irreversible (plastic) deformation, were observed only when bond angle distributions larger than 13° were reached during loading.

V. DISCUSSION

Application of the Raman spectroscopy-enhanced IIT method demonstrated here enabled mapping of the stressed zone under a spherical tip during indentation loading of a-Si. Detailed analyses of the individual spectra within such maps allowed for quantification of the volumetric strain as well as the structural order in terms of bond angle distortions. This novel *in situ* mapping of the plastic deformation of as-implanted a-Si yields new insight into the deformation and phase transformation behavior of this particular form of a-Si under indentation loading. In particular, comparisons of the mapping results with simulations and other measurements of indentation of a-Si allow the key findings to be interpreted and are discussed here. Some caveats are in order in making these comparisons. The deformation and transformation pathways observed in simulations of a-Si indentation depend sensitively on the interatomic potential used and on the initial simulation configuration of the a-Si (e.g., relaxed versus unrelaxed). In indentation experiments, the deformation and transformation pathways observed also depend on the initial configuration (e.g., annealed versus as-implanted a-Si) and on the geometry and scale of the indentation, as these determine the hydrostatic/shear stress ratio. Finally, in DAC or related tests, different test configurations and confining media also lead to different and perhaps unknown hydrostatic/shear stress ratios. Nonetheless, a broad picture of the probable structures developed during the indentation loading sequence in these experiments can be formed, as summarized in Fig. 7. More detailed analyses will appear in a future paper.

In simulation studies by Durandurdu and Drabold, the exposure of a-Si to hydrostatic pressure led to compression (densification) of the network characterized by local changing of the tetrahedral angles and shortened bond lengths in the Si tetrahedra (without changing coordination) [39]. These changes resulted in a continuous broadening of the bond angle distribution [39]. In the paper here, the applied indentation load (hydrostatic pressure + shear stress) led to compression of the sample material inside a contact zone beneath the tip, as indicated by the negative volumetric strain values [see Fig. 6(a)]. Increases in the bond angle distribution, as reported in the simulation studies, were also observed at loads greater than L1 in the *in situ* experiments [see Fig. 6(b)].

Greater hydrostatic pressures in other simulation studies initiated the formation of defects in the Si tetrahedra, with local changes in the coordination within the a-Si network [27,39,55]. Modifications of the average coordination seemed to start when the strained network exhibited bond angle distributions of about 12.9° [39]. Coordination defects include fivefold coordinated atoms (or floating bonds) with smaller energies required for their formation than threefold coordinated defects (or dangling bonds) [10]. Morishita described the fivefold coordinated arrangement as a slightly deformed tetrahedral structure: Four neighboring atoms with a fifth atom, initially located outside the first coordination shell, moved into an interstitial position of the tetrahedron [59]. Significant growth in the population of fivefold coordinated atoms was observed in simulations when the a-Si network was exposed to strains above a certain threshold (which may be affected by temperature and shear velocity) [2]. In theoretical studies, an increase

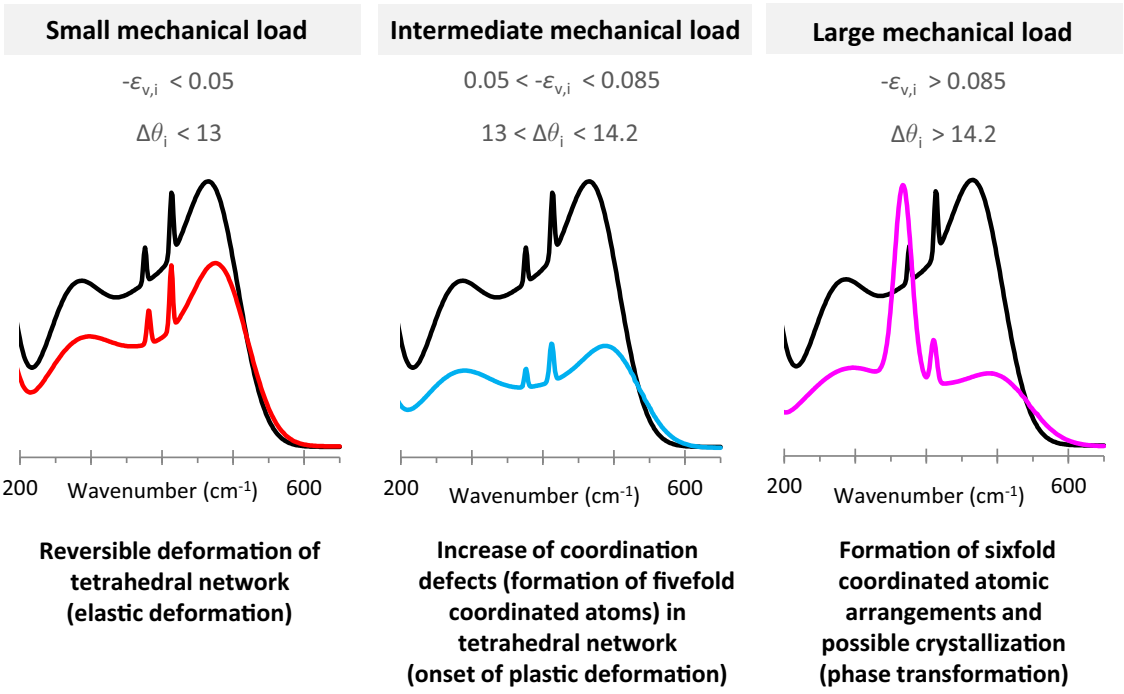

FIG. 7. (Color online) Summary of the deformation mechanisms of a-Si thin film during mechanical loading induced by indentation. The black colored curves represent a characteristics Raman spectrum from the pristine (untested samples), whereas the colored curves shows a Raman spectrum collected under the various mechanical loads. The data given for the negative (compressive) volumetric strain, $\varepsilon_{V,i}$ and the bond angle distribution, $\Delta\theta_i$, refer to the threshold values found for the experimental conditions employed in the presented paper.

in the number of fivefold coordinated atoms has been linked to losses in intensity [7,15,24,27,55] and widening of the TO band [6,24,27,55]. In the present paper, a decrease in the relative intensity of the TO band [see Fig. 5(b)] and a sizable change in the width (see Fig. 6) was observed at load L3. At this load, strains of 0.05 and greater were first observed in the strained amorphous network. Following the previously mentioned observations, this would suggest the formation of fivefold coordinated atoms in the strained amorphous material at load L3.

The presence of fivefold coordinated atoms has been deemed essential for the plastic deformation of a-Si [1,33], in which fivefold coordinated atoms, or so called liquidlike particles, act as plasticity carriers for a-Si in analogy with dislocations in crystalline Si [1]. Assuming the validity of this proposition, the spectral changes observed before the occurrence of fivefold coordinated atoms (indicated by bond angle deviations larger than 13° and strains greater than 0.05) would be linked to elastic (reversible) modifications of the a-Si network in the indented zone. The load-unload measurements here showed that, indeed, permanent changes in the spectral features were only observed when bond angle distributions larger than 13° and strains greater than 0.05 were reached during loading.

Greater indentation loads and the related increased disorder of, and strains in, the amorphous structure (bond angles larger than 14.2° and strains greater than 0.085) appeared to promote the formation of another crystallographic phase. This phase was indicated by the occurrence of peak 5 in the Raman spectra at indentation loads L4 and L5 [see Figs. 4(e) and 4(f)]. Simulations of hydrostatic compression suggest that large angle distortions yield an increase in the atomic coordination of highly strained structures through transformation to more closely packed geometries [38,39]. The formation of a new phase observed in this experimental study is consistent with these simulations.

For a-Si films, the probability of phase transformation depends on the degree of order, with phase transformation more likely than plastic flow for a high degree of order [43]. An initial bond angle distribution of about 12.2° suggests a relative large degree of structural disorder present in the tested a-Si film (considering that the theoretical bond angle distribution of a highly ordered (highly relaxed) a-Si has been determined to be 7° [18]). This large degree of disorder, which is not surprising given that the ion implanted amorphous films were tested without prior annealing (and were in the unrelaxed state), would suggest deformation by plastic flow. However, it has been also been demonstrated [40] that large enough strains in the material pinned between an indenter probe and the underlying substrate facilitate phase transformation during the indentation of unrelaxed a-Si films. This paper confirmed that observation.

The wavenumber range occupied by the newly formed peak 5 [355 cm^{-1} to 370 cm^{-1}, see Fig. 6(d)] was compared to experimental data and simulation studies [60,61]. It was found that peak 5 aligned very well with the TO mode of the sixfold coordinated β-tin structure of Si. (The second mode associated with β-tin and located at around 120 cm^{-1} [60,61] was outside the detection range of the experimental set up and, therefore, could not be observed in this paper.)

The present paper thus provides experimental evidence for the phase transformation of a-Si to the crystalline β-tin phase during indentation, as has been previously proposed [40,46]. In earlier indentation tests on a-Si films employing *in situ* electrical measurements, changes in the electrical contact resistance indicated the transition from the starting a-Si to a more conductive, metallic structure [40]. However, the exact nature of this metallic phase could not be identified in these experiments. Interestingly, an increase in $I_{LO/TO}$ [Fig. 5(b)] has previously been correlated with an increase in medium range order [62], i.e., structural order beyond $\sim$1 nm. This increase in $I_{LO/TO}$ with increasing pressure could thus be a precursor to potential crystallization into β-tin (suggested by the appearance of the strong band at 360 cm^{-1}). In such a scenario, the disordering of the tetrahedral structure (suggested by the loss of TO intensity) could be correlated to the formation of the sixfold coordinated β-tin.

The crystallization to β-tin has been only infrequently observed during compression of a-Si in DACs [30,55]. As has been very recently pointed out, this is due to the fact that high impurity levels inherent to the samples suppress or retard crystallization processes [30]. Some DAC studies reported a polyamorphic transition [25–27] from the fourfold coordinated to five- and sixfold coordinated amorphous networks [26,27]. The effect of the fivefold coordinated defects on the vibrational spectrum of the a-Si structure has already been described. Sixfold coordinated atoms contribute to Raman modes similar to the TO band of the crystalline β-tin phase [27]. The superposition of the vibrational modes of the differently coordinated Si species leads to a spectrum featuring a single broad peak with a maximum around 400 cm^{-1} [27,63], which is not unlike the Raman spectra observed in this paper. The structural modifications signifying the five- and sixfold amorphous network are similar to modifications observed in the contact zone of the indented a-SoS sample of this paper with the exception of the missing long-range order of sixfold coordinated atoms. The lack of structural order renders the vibrational modes associated with sixfold coordinated Si atoms less well defined than for the crystalline arrangement (β-tin) just as for the amorphous fourfold coordinated Si phase in comparison to its crystalline dc Si-I phase counterpart.

VI. CONCLUSION

The plastic deformation of a-Si thin films under indentation loading (hydrostatic pressure + shear stress) processes were studied by *in situ* Raman imaging of the deformed contact region of a-Si, employing Raman spectroscopy-enhanced IIT. The quantitative analysis enabled by this new technique enabled the evolution of the spatial distribution of various amorphous and crystalline Si phases generated during deformation along with the strain field to be studied. Based on this paper and previously cited literature, the following picture regarding indentation-induced plastic deformation of a-Si thin film emerged (see Fig. 7).

(1) When the mechanical load is initially applied in the indentation test ($p_i < 6.2$ GPa), the induced strains are accommodated by reversible deformation of the tetrahedral network (local changing of bond angles and shortening of bond lengths) without modification to the original atomic coordination of the network.

(2) At greater mechanical loads (6.2 GPa $\geqslant p_i <$ 8.2 GPa), the increased distortions (disorder) of the tetrahedral network lead to formation of more closely packed atomic arrangements, at first in the form of predominately fivefold coordinated defects. The occurrence of fivefold coordinated defects during indentation seems to mark the onset of irreversible structural alterations, and thus the beginning of plastic deformation of the a-Si thin film.

(3) Further increase in the indentation load ($p_i \geqslant$ 8.2 GPa) seems to initiate the formation of sixfold coordinated atomic arrangements. Under certain conditions, these sixfold coordinated arrangements may develop a long-range order and nucleate as crystalline β-tin phase within the a-Si network. If crystallization does not take place, the deformed material under the indenter probe maintains its amorphous tetrahedral structure with a high density of coordination defects.

(4) The formation of eight- or ninefold coordinated atomic arrangements, as reported in theoretical and experimental studies under quasihydrostatic conditions, was not observed as the required pressure was beyond that attainable in these indentation tests. (It should be noted that the parameter ranges given in this summary and in Fig. 7 can be considered as estimates only. More detailed experiments are required to quantify and validate the boundary values more precisely for the different deformation mechanisms.)

The reported *in situ* experiments provide insights into the plastic deformation of a-Si during indentation loading, confirming, and providing experimental evidence for, some of the previous assumptions made on this subject. In this context, the developed experimental setup coupling indentation with *in situ* Raman microscopy has shown potential in advancing the understanding of deformation mechanisms and will provide a very useful tool in validating and refining contact models and related simulation studies.

ACKNOWLEDGMENTS

B.H. gratefully acknowledges current funding from an Alvin M. Weinberg Fellowship (ORNL) and the Spallation Neutron Source (ORNL), sponsored by the U.S. Department of Energy, Office of Basic Energy Sciences. ORNL is funded under DOE-BES Contract No. DE-AC05-00OR22725, the SNS is supported by the Scientific User Facilities division, DOE-BES under Contract No. DE-AC05-00OR22725 and the Alvin M. Weinberg Fellowship by the ORNL LDRD scheme under Project No. 7620.

[1] M. J. Demkowicz and A. S. Argon, Liquidlike atomic environments act as plasticity carriers in amorphous silicon, Phys. Rev. B **72**, 245205 (2005).

[2] A. Kerrache, N. Mousseau, and L. J. Lewis, Amorphous silicon under mechanical shear deformations: Shear velocity and temperature effects, Phys. Rev. B **83**, 134122 (2011).

[3] C. Fusco, T. Albaret, and A. Tanguy, Role of local order in the small-scale plasticity of model amorphous materials, Phys. Rev. E **82**, 066116 (2010).
[4] D. Beeman, R. Tsu, and M. F. Thorpe, Structural information from the Raman spectrum of amorphous silicon, Phys. Rev. B **32**, 874 (1985).
[5] J. Fabian and P. B. Allen, Thermal Expansion and Grüneisen Parameters of Amorphous Silicon: A Realistic Model Calculation, Phys. Rev. Lett. **79**, 1885 (1997).
[6] F. Finkemeier and W. von Niessen, Phonons and phonon localization in a-Si: Computational approaches and results for continuous-random-network-derived structures, Phys. Rev. B **58**, 4473 (1998).
[7] K. Ishibashi, K. Tsumuraya, and S. Nakata, Local vibrational densities of states in glasses: Numerical study of a model of amorphous silicon, J. Chem. Phys. **101**, 1412 (1994).
[8] T. Ishidate, K. Inoue, K. Tsuji, and S. Minomura, Raman scattering in hydrogenated amorphous silicon under high pressure, Solid State Comm. **42**, 197 (1982).
[9] M. Ishimaru, Atomistic simulations of structural relaxation processes in amorphous silicon, J. Appl. Phys. **91**, 686 (2002).
[10] P. C. Kelires and J. Tersoff, Glassy Quasithermal Distribution of Local Geometries and Defects in Quenched Amorphous Silicon, Phys. Rev. Lett. **61**, 562 (1988).
[11] J. S. Lannin, L. J. Pilione, S. T. Kshirsagar, R. Messier, and R. C. Ross, Variable structural order in amorphous silicon, Phys. Rev. B **26**, 3506 (1982).
[12] V. A. Luchnikov, N. N. Medvedev, A. Appelhagen, and A. Geiger, Medium-range structure of amorphous silicon studied by the Voronoi-Delaunay method, Mol. Phys. **88**, 1337 (1996).
[13] N. Maley, D. Beeman, and J. S. Lannin, Dynamics of tetrahedral networks: Amorphous Si and Ge, Phys. Rev. B **38**, 10611 (1988).
[14] M. Marinov and N. Zotov, Model investigation of the Raman spectra of amorphous silicon, Phys. Rev. B **55**, 2938 (1997).
[15] N. Mousseau and L. J. Lewis, Dynamical models of hydrogenated amorphous silicon, Phys. Rev. B **43**, 9810 (1991).
[16] S. Muthmann, F. Köhler, R. Carius, and A. Gordijn, Structural order on different length scales in amorphous silicon investigated by Raman spectroscopy, Phys. Status Solidi A **207**, 544 (2010).
[17] D. E. Polk and D. S. Boudreaux, Tetrahedrally Coordinated Random-Network Structure, Phys. Rev. Lett. **31**, 92 (1973).
[18] R. Tsu, J. G. Hernandez, and F. H. Pollak, Determination of energy barrier for structural relaxation in a-Si and a-Ge by Raman scattering, J. Non-Cryst. Solids **66**, 109 (1984).
[19] R. Tsu, J. Gonzalez-Hernandez, J. Doehler, and S. R. Ovshinsky, Order parameters in a-Si systems, Solid State Comm. **46**, 79 (1983).
[20] R. L. C. Vink, G. T. Barkema, and W. F. van der Weg, Raman spectra and structure of amorphous Si, Phys. Rev. B **63**, 115210 (2001).
[21] K. Winer, Structural and vibrational properties of a realistic model of amorphous silicon, Phys. Rev. B **35**, 2366 (1987).
[22] C. K. Wong and G. Lucovsky, Bond angle disorder in tetrahedrally bonded amorphous silicon, in *Materials Issues in Amorphous-semiconductor Technology, Symposium Held April 15–18, 1986, Paolo Alto, California, USA* (Materials Research Society, Pittsburg, 1986), vol. 70, p. 77.
[23] P. X. Zhang, I. V. Mitchell, B. Y. Tong, P. J. Schultz, and D. J. Lockwood, Depth-dependent disordering in a-Si produced by self-ion-implantation, Phys. Rev. B **50**, 17080 (1994).
[24] N. Zotov, M. Marinov, N. Mousseau, and G. Barkema, Dependence of the vibrational spectra of amorphous silicon on the defect concentration and ring distribution, J. Phys.: Condens. Matter **11**, 9647 (1999).
[25] O. Shimomura, S. Minomura, N. Sakai, K. Asaumi, K. Tamura, J. Fukushima, and H. Endo, Pressure-induced semiconductor-metal transitions in amorphous Si and Ge, Phil. Mag. **29**, 547 (1974).
[26] D. Daisenberger, M. Wilson, P. F. McMillan, R. Quesada Cabrera, M. C. Wilding, and D. Machon, High-pressure x-ray scattering and computer simulation studies of density-induced polyamorphism in silicon, Phys. Rev. B **75**, 224118 (2007).
[27] P. F. McMillan, M. Wilson, D. Daisenberger, and D. Macon, A density-driven phase transition between semiconducting and metallic polyamorphs of silicon, Nat. Mater. **4**, 680 (2005).
[28] K. K. Pandey, N. Garg, K. V. Shanavas, S. M. Sharma, and S. K. Sikka, Pressure induced crystallization in amorphous silicon, J. Appl. Phys. **109**, 113511 (2011).
[29] M. Imai, T. Mitamura, K. Yaoita, and K. Tsuji, Pressure-induced phase transition of crystalline and amorphous silicon and germanium at low temperatures, High Press. Res. **15**, 167 (1996).
[30] B. Haberl, M. Guthrie, D. Sprouster, J. Williams, and J. Bradby, New insight into pressure-induced phase transitions of amorphous silicon: the role of impurities, J. Appl. Cryst. **46**, 758 (2013).
[31] W. A. Bassett, Deviatoric stress: a nuisance or a gold mine?, J. Phys.: Condens. Matter **18**, S921 (2006).
[32] S. Klotz, J.-C. Chervin, P. Munsch, and G. Le Marchand, Hydrostatic limits of 11 pressure transmitting media, J. Phys. D **42**, 075413 (2009).
[33] M. J. Demkowicz and A. S. Argon, Autocatalytic avalanches of unit inelastic shearing events are the mechanism of plastic deformation in amorphous silicon, Phys. Rev. B **72**, 245206 (2005).
[34] M. Talati, T. Albaret, and A. Tanguy, Atomistic simulations of elastic and plastic properties in amorphous silicon, EPL **86**, 66005 (2009).
[35] A. Kerrache, N. Mousseau, and L. J. Lewis, Crystallization of amorphous silicon induced by mechanical shear deformations, Phys. Rev. B **84**, 014110 (2011).
[36] A. S. Argon and M. J. Demkowicz, Atomistic simulation and analysis of plasticity in amorphous silicon, Phil. Mag. **86**, 4153 (2006).
[37] K. V. Shanavas, K. K. Pandey, N. Garg, and S. M. Sharma, Computer simulations of crystallization kinetics in amorphous silicon under pressure, J. Appl. Phys. **111**, 063509 (2012).
[38] M. Durandurdu and D. A. Drabold, Ab initio simulation of first-order amorphous-to-amorphous phase transition of silicon, Phys. Rev. B **64**, 014101 (2001).
[39] M. Durandurdu and D. A. Drabold, Ab initio simulation of pressure-induced low-energy excitations in amorphous silicon, Phys. Rev. B **66**, 155205 (2002).
[40] B. Haberl, J. E. Bradby, S. Ruffell, J. S. Williams, and P. Munroe, Phase transformations induced by spherical indentation in ion-implanted amorphous silicon, J. Appl. Phys. **100**, 013520 (2006).
[41] S. Ruffell, J. Vedi, J. E. Bradby, and J. S. Williams, Effect of hydrogen on nanoindentation-induced phase transformations in amorphous silicon, J. Appl. Phys. **106**, 123511 (2009).

[42] S. Ruffell, J. Vedi, J. E. Bradby, J. S. Williams, and B. Haberl, Effect of oxygen concentration on nanoindentation-induced phase transformations in ion-implanted amorphous silicon, J. Appl. Phys. **105**, 083520 (2009).

[43] L. B. Bayu Aji, S. Ruffel, B. Haberl, J. E. Bradby, and J. S. Williams, Correlation of indentation-induced phase transformations with the degree of relaxation of ion-implanted amorphous silicon, J. Mater. Res. **28**, 1056 (2013).

[44] D. R. Clarke, M. C. Kroll, P. D. Kirchner, R. F. Cook, and B. J. Hockey, Amorphization and Conductivity of Silicon and Germanium Induced by Indentation, Phys. Rev. Lett. **60**, 2156 (1988).

[45] S. Ruffell, J. E. Bradby, J. S. Williams, and P. Munroe, Formation and growth of nanoindentation-induced high pressure phases in crystalline and amorphous silicon, J. Appl. Phys. **102**, 065321 (2007).

[46] M. M. Khayyat, G. K. Banini, D. G. Hasko, and M. M. Chaudhri, Raman microscopy investigations of structural phase transformations in crystalline and amorphous silicon due to indentation with a Vickers diamond at room temperature and at 77 K, J. Phys. D: Appl. Phys. **36**, 1300 (2003).

[47] V. I. Ivashchenko, P. E. A. Turchi, and V. I. Shevchenko, Simulations of indentation-induced phase transformations in crystalline and amorphous silicon, Phys. Rev. B **78**, 035205 (2008).

[48] Y. B. Gerbig, C. A. Michaels, A. M. Forster, J. W. Hettenhouser, W. E. Byrd, D. J. Morris, and R. F. Cook, Indentation device for in situ Raman spectroscopic and optical studies, Rev. Sci. Instrum. **83**, 125106 (2012).

[49] Y. B. Gerbig, C. A. Michaels, and R. F. Cook, In situ observation of the spatial distribution of crystalline phases during pressure-induced transformations of indented silicon thin films, J. Mater. Res. **30**, 390 (2015).

[50] Any mention of commercial products within this paper is for information only; it does not imply recommendation or endorsement by NIST.

[51] B. Haberl, S. N. Bogle, T. Li, I. McKerracher, S. Ruffell, P. Munroe, J. S. Williams, J. R. Abelson, and J. E. Bradby, Unexpected short- and medium-range atomic structure of sputtered amorphous silicon upon thermal annealing, J. Appl. Phys. **110**, 096104 (2011).

[52] D. L. Williamson, S. Roorda, M. Chicoine, R. Tabti, P. A. Stolk, S. Acco, and F. W. Saris, On the nanostructure of pure amorphous silicon, Appl. Phys. Lett. **67**, 226 (1995).

[53] P. Roura, J. Farjas, and P. Roca i Cabarrocas, Quantification of the bond-angle dispersion by Raman spectroscopy and the strain energy of amorphous silicon, J. Appl. Phys. **104**, 073521 (2008).

[54] A. Battaglia, S. Coffa, F. Priolo, G. Compagnini, and G. A. Baratta, Low-temperature modifications in the defect structure of amorphous silicon probed by in situ Raman spectroscopy, Appl. Phys. Lett. **63**, 2204 (1993).

[55] D. Daisenberger, T. Deschamps, B. Champagnon, M. Mezouar, R. Q. Cabrera, M. Wilson, and P. F. McMillan, Polyamorphic amorphous silicon at high pressure: Raman and spatially resolved X-ray scattering and molecular dynamics studies, J. Phys. Chem. B **115**, 14246 (2011).

[56] M. Kadleíková, J. Breza, and M. Veselý, Raman spectra of synthetic sapphire, Microelectr. J. **32**, 955 (2001).

[57] A. J. M. Berntsen, W. F. van der Weg, P. A. Stolk, and F. W. Saris, Separating the effects of hydrogen and bond-angle variation on the amorphous-silicon band gap, Phys. Rev. B **48**, 14656 (1993).

[58] S. Kim, S. H. Choi, C. J. Park, H. Y. Cho, and R. G. Elliman, Luminescence study of Si^- and Ge^- implanted (1102) sapphires, J. Korean Phys. Soc. **45**, S501 (2004).

[59] T. Morishita, High Density Amorphous Form and Polyamorphic Transformations of Silicon, Phys. Rev. Lett. **93**, 055503 (2004).

[60] H. Olijnyk, Raman scattering in metallic Si and Ge up to 50 GPa, Phys. Rev. Lett. **68**, 2232 (1992).

[61] K. Gaál-Nagy, M. Schmitt, P. Pavone, and D. Strauch, Ab initio study of the high-pressure phase transition from the cubic-diamond to the β-tin structure of Si, Comput. Mater. Sci. **22**, 49 (2001).

[62] J. E. Gerbi, P. M. Voyles, M. M. J. Treacy, J. M. Gibson, and J. R. Abelson, Increasing medium-range order in amorphous silicon with low-energy ion bombardment, Appl. Phys. Lett. **82**, 3665 (2003).

[63] S. K. Deb, M. Wilding, M. Somayazulu, and P. F. McMillan, Pressure-induced amorphization and an amorphous-amorphous transition in densified porous silicon, Nature **414**, 528 (2001).